Port-Hamiltonian reduced order modelling of the 2D Maxwell equations

Mattéo Gouzien, Charles Poussot-Vassal, Ghislain Haine and Denis Matignon
Fédération ENAC ISAE-SUPAERO ONERA, Université de Toulouse, Toulouse, France

COMPEL - The international journal for computation and mathematics in electrical and electronic engineering

Abstract

Purpose – This study aims to develop a systematic and efficient method for modeling and reducing the computational complexity of the Maxwell equations in 2D. By maintaining the port-Hamiltonian structure in both the full order model (FOM) and reduced-order model (ROM), this approach ensures that the essential dynamical properties are preserved. The ultimate goal is to create a reduced order model that is suitable for rapid simulations, control and analysis in electromagnetic applications, such as waveguides, which involve boundary control and observation, as well as interface discontinuities.

Design/methodology/approach – This research introduces an ROM procedure for the 2D Maxwell equations within a port-Hamiltonian framework. Using a mixed finite element method, the high-fidelity FOM is generated, which retains the original structure of the Maxwell equations. Model reduction is then achieved through the Loewner framework, allowing for a low-complexity model that is computationally efficient while preserving the port-Hamiltonian properties. A lifting operator is employed to recover the FOM's internal variables from the reduced model, validating the accuracy of the ROM in reproducing the FOM's dynamic behavior.

Findings – The proposed methodology effectively reduces the dimension of the Maxwell system by approximately 35 times, significantly decreasing computational time while maintaining high fidelity in the key output responses. Simulation results demonstrate that the reduced model accurately replicates the full order model's dynamics and power balance. The approach also highlights the advantages of using a port-Hamiltonian structure for energy tracking, with ROMs exhibiting only minor discrepancies due to truncation. The findings validate the ROM as a reliable and efficient approximation of the original high-dimensional system, suitable for complex electromagnetic configurations.

Originality/value – This work provides a novel approach to reducing the 2D Maxwell equations within a port-Hamiltonian framework, preserving essential structure and dynamical properties. By leveraging the Loewner framework with a unique focus on passivity preservation, the method offers a practical solution for efficient simulation and control in electromagnetic systems. This ROM methodology, with its reduced computational burden and enhanced accuracy, is valuable for applications in electromagnetic field simulations and control design, where high computational efficiency and structure preservation are critical [1].

Keywords Reduced order method, Electromagnetic waves, Finite element method, Model order reduction, Partial differential equations, Waveguides

Paper type Research paper

Received 17 October 2024
Revised 1 April 2025
Accepted 27 May 2025

The authors would like to thank Pierre Vuillemin from ONERA for the careful computation of the projectors, Michel Fournié from ISAE-SUPAERO for his expertise on GetFEM and Romain Pascaud from ISAE-SUPAERO for fruitful discussions on the waveguide and on more elaborate test cases in electromagnetic.

Funding: This work was funded by Agence de l'innovation de Défense No. FAMAS Project.

COMPEL - The international journal for computation and mathematics in electrical and electronic engineering
© Emerald Publishing Limited
0332-1649
DOI 10.1108/COMPEL-10-2024-0421

1. Introduction

In aerospace engineering, solving Maxwell's equations is essential for accurate electromagnetic analysis of systems such as antennas, radar cross-section calculations and stealth technology design. The present work is motivated by an efficient numerical representation of the Maxwell's equation on a 2D domain Ω, with actuators and sensors that are *collocated* at the boundary $\partial\Omega$; the partial differential equation (PDE) model is first described as a distributed port-Hamiltonian (pH) system [see *e.g.* van der Schaft and Maschke (2002) and Rashad *et al.* (2020) for a recent overview], second discretized in a structure-preserving manner thanks to a particular instance of the mixed finite element method (MFEM) (Cardoso-Ribeiro *et al.*, 2021). Although in 1D with physical parameters which are uniform in space, the input-output transfer function of a wave equation would be easy to compute, the task becomes more difficult with varying parameters, see e.g. Condon (2024). In a generic geometric 2D domain with heterogeneous and anisotropic parameters, and even more in the case of the Maxwell system, it is almost impossible. However, a high-fidelity and complex full order model (FOM), taking all these important properties into account, can be computed at the discrete level thanks to the partitioned finite element method (PFEM) following Cardoso-Ribeiro *et al.* (2021), which can be efficiently simulated using SCRIMP [2], a dedicated Python package, see Ferraro *et al.* (2024).

The FOM results in a finite-dimensional linear pH system, embedding a very large number of internal state variables, a relatively large number of inputs and outputs. Such a high dimension is a limiting factor for simulation, optimization, analysis and control. Easy-to-use dynamical models (e.g. in a many query simulation-based process), reducing the computational burden, is one purpose of the model approximation and reduction discipline. The goal is to approximate the original system with a smaller and simpler system with the *same structure* and similar response characteristics as the original, the low-complexity model, also called a reduced-order model (ROM).

Hence, we seek to compute an ROM while imposing the port-Hamiltonian structure. Many benefits lie in the preservation of this structure, they will be detailed later. Most notably, the state of the port-Hamiltonian ROM holds significant importance from an energy perspective. Indeed, the pH structure provides three major benefits:

(1) the different energies can be analyzed (and physical characteristics can be extracted from the pH form);

(2) the original model structure is preserved (passivity), which is convenient for physicists; and

(3) the structure allows one to keep the interpretability of the variables.

As an illustration of the capabilities of the method, we provide here Figure 1, which shows the a snapshot of the time-domain simulation results of the FOM compared to the ROM obtained by the following procedure of § 4, which has 13 times less degrees of freedom and a computational time almost 100 times faster.

The key point of this work is to guarantee the preservation of the port-Hamiltonian structure along the following three steps: modeling, discretization, model order reduction.

The use of pH framework for electrical network is not new, see e.g. Bartel and Günther (2018) for a review, Gernandt *et al.* (2021) for the port-Hamiltonian setting, and Márquez *et al.* (2020) for the implementation using Modelica. For full wave electromagnetics, one can refer to van der Schaft and Maschke (2002) for a presentation of Maxwell's equations as a pHs, to Ciuprina *et al.* (2022) for a formulation with boundary conditions as ports together with the use of the finite elements method (FEM), also to Clemens and Weiland (2001) for the presentation a finite integration technique (FIT), which has the property of structure-

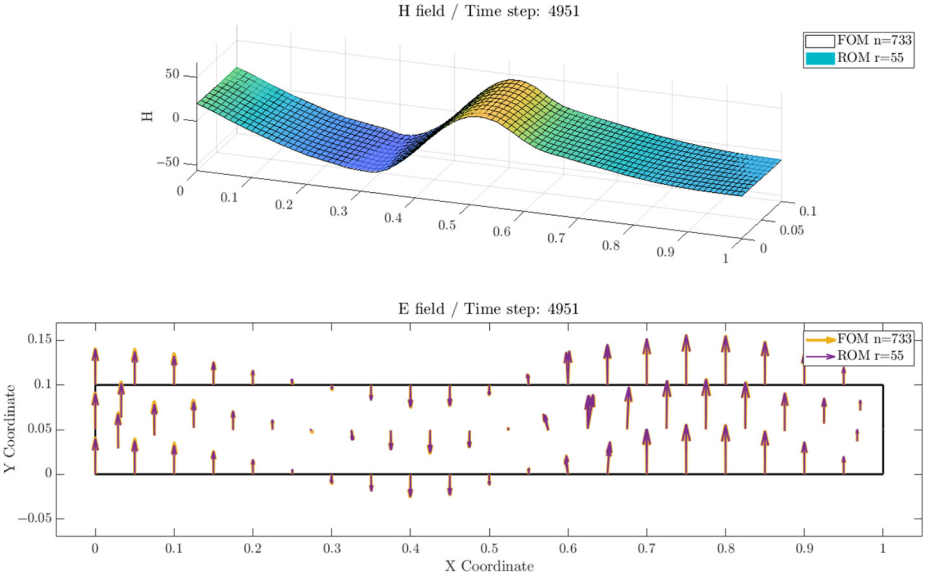

Figure 1. Snapshot of magnetic and electric fields of the full order model (FOM) of dimension $n = 733$ and obtained reduced order model (ROM) of size $r = 55$
Source: Authors' own work

preservation; finally Bartel *et al.* (2024) shows some recent applications of these techniques to coupled systems, and Bundschuh *et al.* (2023) provides a platform-independent simulation software for various electromagnetic and thermal field problems. Now as far as model order reduction (MOR) is concerned, the use of the Loewner framework has been successfully applied to models of PDEs in 1D, first in Cherifi and Brugnoli (2021) and recently Toledo-Zucco *et al.* (2024b), an attempt to tackle PDEs in 2D was made in Poussot-Vassal *et al.* (2023) for the wave *equation.*

1.1 Outline

The paper is organized as follows: writing the classical Maxwell equations as an infinite-dimensional pH system, both in 3D and in 2D, is presented in § 2; based on this, passing from the *distributed-parameter* pH system to a *lumped-parameter* pH system of high dimension while keeping the underlying structure is detailed in § 3, with the use of the PFEM; then, § 4 explains how to obtain a low-dimensional pH system, using the Loewner framework. The test case of a waveguide is worked out in § 5. Finally, some conclusions are drawn and some perspectives are sketched in the § 6.

In addition, time-domain simulation videos of the results obtained with the proposed pH-ROM construction are available at the following links: https://youtu.be/ORhRz1hT_Ak (electric and magnetic fields) and https://youtu.be/MtazBkkQQc0 (run with mismatch error over the full mesh).

1.2 Notations and preliminaries

The set of real and complex numbers of dimension n are denoted, respectively by $\mathbb{R}^n$ and $\mathbb{C}^n$. The complex variable $\imath = \sqrt{-1}$. The notation $\mathbb{X}^n_\Lambda : \{x \in \mathbb{X}^n \backslash \Lambda\}$, where Λ denotes a finite

number set (typically singularities) in $\mathbb{X}^n$ ($\mathbb{X}^n = \{\mathbb{R}^n, \mathbb{C}^n\}$). We denote $X^\top$ and X^H the transpose and transpose conjugate of matrix X, respectively. Identity matrix of dimension p reads I_p and $m \times p$ rectangular (resp. m square) null matrix is denoted $0_{m,p}$ (resp. 0_m). The Laplace variable is denoted $s \in \mathbb{C}$. Along the paper, we will consider multi-input multi-output (MIMO) linear time invariant (LTI) continuous-time dynamical systems realizations (with $\mathbf{x}(0) = 0$) of one of this kind:

$$E\dot{\mathbf{x}}(t) = A\mathbf{x}(t) + B\mathbf{u}(t), \;\; \mathbf{y}(t) = C\mathbf{x}(t), \tag{1a}$$

$$\mathbf{x}(t) = A\mathbf{x}(t) + B\mathbf{u}(t), \;\; \mathbf{y}(t) = C\mathbf{x}(t) + D\mathbf{x}(t)\,, \text{ or} \tag{1b}$$

$$M\dot{\mathbf{x}}(t) = (J-R)Q\mathbf{x}(t) + (G-P)\mathbf{u}(t), \;\; \mathbf{y}(t) = (G+P)^\top Q\mathbf{x}(t) + (N+S)\mathbf{u}(t), \tag{1c}$$

where $\mathbf{x}(t) \in \mathbb{R}^n$ and $\mathbf{u}(t)$, $\mathbf{y}(t) \in \mathbb{R}^m$ are vector-valued functions denoting the internal variables, input and output of the system. In the standard descriptor (1a) and non-descriptor (1b) forms, we consider constant matrices $E, A \in \mathbb{R}^{n\times n}$, $B, C^\top \in \mathbb{R}^{n\times m}$ and $D \in \mathbb{R}^{m\times m}$. When considering the pH form (1c), $M, J, R, Q \in \mathbb{R}^{n\times n}$, $G, P \in \mathbb{R}^{n\times m}$ and $N, S \in \mathbb{R}^{m\times m}$. For brevity, (1a) and (1b) are denoted $\mathbf{\Sigma} := (E, A, B, C, 0_m)$ and $\mathbf{\Sigma} := (In, A, B, C, D)$ respectively. The pH form (1c) is shortly denoted $\mathbf{\Sigma}_{\text{pH}} := (M, Q, J, R, G, P, N, S)$.

By introducing the co-energy variable $M\mathbf{e}(t) = Q\mathbf{x}(t)$, (1c) boils down to $\widetilde{M}\mathbf{e}(t) = (J-R)\mathbf{e}(t) + (G-P)\mathbf{u}(t)$ and $\mathbf{y}(t) = (G+P)^\top\mathbf{e}(t) + (N+S)\mathbf{u}(t)$, where $\widetilde{M} \simeq Q^{-1}M$ is another $\mathbb{R}^{n\times n}$ matrix. The latter is the so-called *co-energy formulation of the pH system*, and is of specific interest in the numerical simulation. This interest will be enlightened in § 3.

In each case, we define the associated transfer functions as $\mathbf{H}$: $\mathbb{C}_\Lambda \to \mathbb{C}^{m\times m}$, where $\mathbf{H}(s) = C(sE - A)^{-1}B$ for (1a), $\mathbf{H}(s) = C(sI - A)^{-1}B + D$ for (1b) and $\mathbf{H}(s) = (G+P)^\top Q(sM - (J-R)Q)^{-1}(G-P) + (N+S)$ for (1c) [3]. On the basis of $\mathbf{H}$, let us also denote the spectral density as $\mathbf{\Phi}_\mathbf{H}(s) := \mathbf{H}(s) + \mathbf{H}^\top(-s)$. In addition, for sake of completeness and to characterize a pH system, we refer the reader to Definitions 2.1, 2.2 and 2.3 from Benner *et al.* (2020).

2. The Maxwell system as a port-Hamiltonian system

The objective of this section is to recall how Maxwell's equations of electromagnetism can be recast into the pH formalism (Farle *et al.*, 2013; Payen *et al.*, 2020; Haine *et al.*, 2022).

Let Ω be a bounded connected set. The Hamiltonian of the system under consideration is the total electromagnetic energy, given by:

$$\mathcal{H}(\mathbf{D}, \mathbf{B}) := \frac{1}{2}\int_\Omega \left(\frac{\mathbf{D}\cdot\mathbf{D}}{\epsilon(\mathbf{x})} + \frac{\mathbf{B}\cdot\mathbf{B}}{\mu(\mathbf{x})}\right). \tag{2}$$

Electric and magnetic *inductions* $\mathbf{D}$ and $\mathbf{B}$ are chosen as energy variables; then computing the variational derivatives of the Hamiltonian $\mathcal{H}$ with respect to them, the electric and magnetic *fields*:

$$\mathbf{E} := \delta_\mathbf{D}\mathcal{H}, \quad \text{and} \quad \mathbf{H} := \delta_\mathbf{B}\mathcal{H}, \tag{3}$$

naturally appear as *co-energy variables*.

The constitutive laws linking them involve the electric permittivity $\epsilon(\mathbf{x})$ and the magnetic permeability $\mu(\mathbf{x})$, and read:

$$\mathbf{D} = \epsilon(\mathbf{x})\mathbf{E}, \quad \text{and} \quad \mathbf{B} = \mu(\mathbf{x})\mathbf{H}. \tag{4}$$

With these notations at hand, the two dynamical Maxwell's equation (known as Maxwell-Ampère and Maxwell-Faraday) can be written as:

$$\begin{cases} \partial_t \mathbf{D} = & \mathbf{curl}\mathbf{H} - \mathbf{J}, \\ \partial_t \mathbf{B} = & -\mathbf{curl}\mathbf{E}. \end{cases} \tag{5}$$

Moreover, $\mathbf{J}$ stands for the total inner distributed current: Ohm's law states that $\mathbf{J} = \sigma\mathbf{E}$, with $\sigma(\mathbf{x})$ the conductivity, responsible of the so-called Joule's effect.

Remark 1. In this work, we do not consider the two other static equations explicitly, namely Maxwell-Gauß $\mathrm{div}\mathbf{D} = \rho$ in presence of a charge density ρ, or Maxwell-flux $\mathrm{div}\mathbf{B} = 0$. Both these equations add algebraic constraints on the solutions which should be taken in account; nevertheless, if the initial data fulfill these constraints, they will be satisfied along the solutions of the infinite-dimensional dynamical system, see e.g., Weiss and Staffans (2013).

Using definition (2), dynamic equations (5) and Stokes identity, one can compute the electromagnetic power as follows:

$$\begin{aligned} \frac{d\mathcal{H}}{dt} &= \int_\Omega \mathbf{E}\cdot\partial_t\mathbf{D} + \mathbf{H}\cdot\partial_t\mathbf{B}, \\ &= \int_\Omega (\mathbf{E}\cdot\mathbf{curl}\mathbf{H} - \mathbf{H}\cdot\mathbf{curl}\mathbf{E}) - \int_\Omega \mathbf{E}\cdot\mathbf{J}, \\ &= -\int_\Omega \mathrm{div}(\mathbf{E}\wedge\mathbf{H}) - \int_\Omega \mathbf{E}\cdot\mathbf{J}, \\ &= -\int_{\partial\Omega} \big(\gamma(\mathbf{E}\wedge\mathbf{H})\big)\cdot\mathbf{n} - \int_\Omega \mathbf{E}\cdot\mathbf{J}, \end{aligned}$$

where γ is the Dirichlet trace operator and $\mathbf{n}$ is the outward normal vector to the boundary $\partial\Omega$.

Making use of $\Pi := \gamma(\mathbf{E}\wedge\mathbf{H})$, the so-called Poynting vector, defined on the boundary $\partial\Omega$, it reads:

$$\frac{d\mathcal{H}}{dt} = -\int_{\partial\Omega} \mathbf{\Pi}\cdot\mathbf{n} - \int_\Omega \mathbf{E}\cdot\mathbf{J}. \tag{6}$$

Thus, the loss of electromagnetic energy comes from the flux of the Poynting vector across the boundary $\partial\Omega$, and the distributed power in the domain Ω, with density $\mathbf{E}\cdot\mathbf{J} = \sigma^{-1}\|\mathbf{J}\|^2 = \sigma\|\mathbf{E}\|^2 \geq 0$, which is actually Joule's effect; this energy is lost in the thermal domain.

Regarding the boundary terms, and in particular the choice of the collocated boundary control $\mathbf{u}$ and observation $\mathbf{y}$, there are several possible choices. The admissibility condition for such choices is that $\int_{\partial\Omega}\mathbf{u}\cdot\mathbf{y} = -\int_{\partial\Omega}\mathbf{\Pi}\cdot\mathbf{n}$.

As main example, we shall concentrate on the 2D Maxwell's equation on a 2D waveguide for sake of simplicity. In that case, Ω is a rectangle in $\mathbb{R}^2$, yielding a *transverse electric* (TE) formulation of Maxwell's equations, which reads:

$$\begin{cases} \partial_t \mathbf{D} &= \mathbf{grad}^{\perp} H_z - \mathbf{J}, \\ \partial_t B_z &= -\operatorname{curl}_{2\mathrm{D}} \mathbf{E}, \end{cases} \tag{7}$$

with, see e.g. (Assous *et al.*, 2018, § 9.2):

$$\mathbf{grad}^{\perp} H_z := \begin{bmatrix} \partial_y H_z \\ -\partial_x H_z \end{bmatrix} = \Theta\, \mathbf{grad}\, H_z,$$

$$\operatorname{curl}_{2\mathrm{D}} \mathbf{E} := \partial_x E_y - \partial_y E_x = \operatorname{div}_{2\mathrm{D}}(\Theta^{\top} \mathbf{E}),$$

where Θ is the rotation of angle $-\frac{\pi}{2}$ rad [4].

Using as *scalar* boundary collocated control and observation:

$$u_\partial := \mathbf{E} \cdot \mathbf{t} \quad \text{and} \quad y_\partial := -H_z, \tag{8}$$

where $\mathbf{t} := \Theta^{\top} \mathbf{n}$ is the tangent vector to $\partial\Omega$. Then, we get the following power balance for the TE 2D Maxwell lossy pH system (7):

$$\frac{d}{dt}\mathcal{H} = -\int_\Omega \mathbf{E} \cdot \sigma \mathbf{E} + \int_{\partial\Omega} u_\partial y_\partial \leq \int_{\partial\Omega} u_\partial y_\partial. \tag{9}$$

3. High fidelity model: a mixed finite element method

To discretize the system (7)–(8) in space, the partitioned finite element method (PFEM) is used, see Cardoso-Ribeiro *et al.* (2021). This method is a particular instance of the robust and well-known mixed finite element method, see Monk (2003), allowing for the discretization of the distributed port-Hamiltonian system into a finite-dimensional port-Hamiltonian system, i.e. in a *structure-preserving* way. The method boils down to three steps:

(1) write a weak formulation of the problem;

(2) use Stokes' identity on a *partition* of the system; and

(3) project on finite sets using finite elements.

Consider systems (7)–(8), multiply by test functions (namely the scalar-valued φ and the vector-valued $\boldsymbol{\varphi}$ defined in Ω, and the scalar-valued ψ defined on $\partial\Omega$), and integrate over Ω:

$$\begin{cases} \displaystyle\int_\Omega \partial_t \mathbf{D} \cdot \boldsymbol{\varphi} = \int_\Omega \mathbf{grad}^{\perp} H_z \cdot \boldsymbol{\varphi} - \int_\Omega \mathbf{J} \cdot \boldsymbol{\varphi}, \\ \displaystyle\int_\Omega \partial_t B_z\, \varphi = -\int_\Omega \operatorname{curl}_{2\mathrm{D}} \mathbf{E} \varphi, \\ \displaystyle\int_{\partial\Omega} y_\partial\, \psi = -\int_{\partial\Omega} H_z \psi. \end{cases}$$

Performing an integration by parts on the second line and substituting the constitutive relations (4) and Ohm's law $\mathbf{J} = \sigma(\mathbf{x})\mathbf{E}$ (i.e. considering the co-energy formulation) lead to the variational formulation:

$$\begin{cases} \displaystyle\int_\Omega \epsilon(\mathbf{x})\partial_t \mathbf{E}\cdot\boldsymbol{\varphi} = \int_\Omega \mathbf{grad}^\perp H_z\cdot\boldsymbol{\varphi} - \int_\Omega \sigma(\mathbf{x})\mathbf{E}\cdot\boldsymbol{\varphi}, \\ \displaystyle\int_\Omega \mu(\mathbf{x})\partial_t H_z\varphi = -\int_\Omega \mathbf{E}\cdot\mathbf{grad}^\perp\varphi - \int_{\partial\Omega} u_\partial\varphi, \\ \displaystyle\int_{\partial\Omega} y_\partial\psi = -\int_{\partial\Omega} H_z\psi. \end{cases} \tag{10}$$

Assume now that you have access to three finite element families $(\boldsymbol{\varphi}^i)_{1\le i\le N_E}$, $(\varphi^k)_{1\le k\le N_H}$, and $(\psi^m)_{1\le m\le N_\partial}$ to discretize respectively $\mathbf{E}$, H_z and the boundary variables: u_∂ and y_∂. This consists in considering the discrete quantities:

$$\mathbf{E}(t,\mathbf{x}) \simeq \mathbf{E}^d(t,\mathbf{x}) := \sum_{i=1}^{N_E} E^i(t)\boldsymbol{\varphi}^i(\mathbf{x}),\ \ \forall t\ge 0,\ \mathbf{x}\in\Omega,$$

$$H_z(t,\mathbf{x}) \simeq H_z^d(t,\mathbf{x}) := \sum_{k=1}^{N_H} H_z^k(t)\varphi^k(\mathbf{x}),\ \ \forall t\ge 0,\ \mathbf{x}\in\Omega,$$

$$u_\partial(t,\mathbf{s}) \simeq u_\partial^d(t,\mathbf{s}) := \sum_{m=1}^{N_\partial} u_\partial^m(t)\psi^m(\mathbf{s}),\ \ \forall t\ge 0,\ \mathbf{s}\in\partial\Omega,$$

and:

$$y_\partial(t,\mathbf{s}) \simeq y_\partial^d(t,\mathbf{s}) := \sum_{m=1}^{N_\partial} y_\partial^m(t)\psi^m(\mathbf{s}),\ \ \forall t\ge 0,\ \mathbf{s}\in\partial\Omega.$$

Substituting them into (10), and considering only the finite element functions as test functions leads to the finite-dimensional linear system:

$$\begin{bmatrix} M_E & 0 & 0 \\ 0 & M_H & 0 \\ 0 & 0 & M_\partial \end{bmatrix} \begin{pmatrix} \underline{\dot E}(t) \\ \underline{\dot H_z}(t) \\ -\underline{y_\partial}(t) \end{pmatrix} = \begin{bmatrix} -R_\sigma & D & 0 \\ -D^\top & 0 & -T \\ 0 & T^\top & 0 \end{bmatrix} \begin{pmatrix} \underline{E}(t) \\ \underline{H_z}(t) \\ \underline{u_\partial}(t) \end{pmatrix}, \tag{11}$$

where the underlined quantities represent the vector of coefficients of an approximation in the appropriate finite element family, e.g. $\underline{E}(t) = \left[E^i(t)\right]_{1\le i\le N_E}$ and so forth, and the matrices are defined as follows:

$$(M_E)_{ij} := \int_\Omega \boldsymbol{\varphi}^j\cdot\epsilon(\mathbf{x})\boldsymbol{\varphi}^i \in \mathbb{R}^{N_E\times N_E},\ \ (M_H)_{k\ell} := \int_\Omega \varphi^\ell\mu(\mathbf{x})\varphi^k \in \mathbb{R}^{N_H\times N_H},$$

$$(M_\partial)_{mn} := \int_{\partial\Omega} \psi^n\psi^m \in \mathbb{R}^{N_\partial\times N_\partial},\ \ (R_\sigma)_{ij} := \int_\Omega \boldsymbol{\varphi}^j\cdot\sigma(\mathbf{x})\boldsymbol{\varphi}^i \in \mathbb{R}^{N_E\times N_E},$$

$$(D)_{i\ell} := \int_\Omega \left(\mathbf{grad}^\perp\varphi^\ell\right)\cdot\boldsymbol{\varphi}^i \in \mathbb{R}^{N_E\times N_H},\ \ (T)_{kn} := \int_{\partial\Omega} \psi^n\gamma(\varphi^n) \in \mathbb{R}^{N_H\times N_\partial}.$$

Equivalently, equation (11) may be easily written under the pH form (1c), more precisely by denoting $n = N_E + N_H$, $m = N_\partial$ (later in §4, m will denote both the size of inputs and outputs) and setting:

$$\mathbf{x} := \begin{pmatrix} -E- \\ \\ -H_z- \end{pmatrix} \in \mathbb{R}^n,\ M := \begin{bmatrix} M_E & 0 \\ \\ 0 & M_H \end{bmatrix} \in \mathbb{R}^{n\times n},\ J := \begin{bmatrix} 0 & D \\ \\ -D^\top & 0 \end{bmatrix} \in \mathbb{R}^{n\times n}, \quad (12)$$

and:

$$R := \begin{bmatrix} R_\sigma & 0 \\ 0 & 0 \end{bmatrix} \in \mathbb{R}^{n\times n},\ G := \begin{bmatrix} 0 \\ -TM_\partial^{-1} \end{bmatrix} \in \mathbb{R}^{n\times m},\ P := 0_{n,m},\ N = S := 0_{m,m},\ Q := I_n, \quad (13)$$

together with $\mathbf{u} := \underline{u_\partial}$ and $\mathbf{y} := \underline{y_\partial}$.

Let us define the discrete Hamiltonian $\mathcal{H}^d$ as the evaluation of the continuous Hamiltonian $\mathcal{H}$ given by (2) in the approximated co-energy variables $\mathbf{E^d}$ and H_z^d. First, we rewrite the continuous Hamiltonian $\mathcal{H}$ as a function of the co-energy variables:

$$\begin{aligned} \mathcal{H}(\mathbf{D}, B_z) :&= \frac{1}{2}\int_\Omega \left(\frac{\mathbf{D}\cdot\mathbf{D}}{\epsilon(\mathbf{x})} + \frac{(B_z)^2}{\mu(\mathbf{x})} \right), \\ &= \frac{1}{2}\int_\Omega \left(\mathbf{E}\cdot\epsilon(\mathbf{x})\mathbf{E} + \mu(\mathbf{x})(H_z)^2 \right), \end{aligned}$$

which easily gives, using the finite element approximations:

$$\begin{aligned} \mathcal{H}^d(\mathbf{E}, H_z) :&= \mathcal{H}\left(\mathbf{E}^d, H_z^d\right), \\ &= \frac{1}{2}\int_\Omega \left(\mathbf{E}^d\cdot\epsilon(\mathbf{x})\mathbf{E}^d + \mu(\mathbf{x})\left(H_z^d\right)^2 \right), \\ &= \frac{1}{2}\left(\underline{E}^\top M_E \underline{E} + \underline{H_z}^\top M_H \underline{H_z} \right). \end{aligned}$$

Then, the power balance reads, at the discrete level:

$$\frac{d}{dt}\mathcal{H}^d = -\underline{E}^\top R_\sigma \underline{E} + \underline{y_\partial}^\top M_\partial \underline{u_\partial} \le \underline{y_\partial}^\top M_\partial \underline{u_\partial}. \quad (14)$$

meaning that the open dynamical system is lossy. Note how it perfectly reproduces the continuous behavior (9). The proof essentially relies on both the symmetric positive-definite matrix on the left of (11) and the skew-symmetric matrix on the right of (11) (multiply both sides of (11) from the left by $\left(\underline{E}^\top, \underline{H_z}^\top, \underline{u_\partial}^\top\right)$ and conclude).

4. Low complexity model in the Loewner framework

Encompassing the large amount ($n = N_E + N_H$) of variables of the high fidelity linear model, constructed in § 3, with a low complexity one, is the purpose of model approximation and reduction research field. One objective of constructing low order

models is to be able to use them in place of the original one for many-query model-based processes such as prediction, health monitoring, control and observer design, analysis. Such an investigation domain is obviously very large, and interested reader may refer to the overview papers Benner *et al.* (2015), Gosea *et al.* (2022) and book from Antoulas *et al.* (2020) for details and references. A standard classification of the model approximation approaches considers either *intrusive* or *non-intrusive* methods. The former requires the model to be accessible while the latter (used-here) only input-output data. In this section, the Loewner Framework (LF) and its extension to passive property (and pH structure) preservation is first recalled. Then, as the original system realization is available, we provide also a projector allowing to recover the original pH-FOM states directly from the time-domain simulation of the simple pH-ROM.

This reduction method stands out particularly because, in addition to guaranteeing the preservation of the geometric structure and the passivity property, the internal energy and power terms of the ROM can be determined solely from state measurements. This advantage provides a great insight into the obtained pH-ROM for analyzing its reliability. Moreover, it allows us to retrieve key interest quantities of the initial model.

4.1 Loewner framework

We first describe the classical LF as exposed in Mayo and Antoulas (2007) and Antoulas *et al.* (2016), as a procedure for building time invariant differential algebraic ROM in the form (1a). Then, its adaptation by Benner *et al.* (2020) to construct a pH-ROM of the form (1c), is recalled.

4.1.1 Interpolation *via* the tangential approach. The nonintrusive LF, introduced in Mayo and Antoulas (2007), offers tools for the reduction, approximation and identification of dynamical systems based on frequency-domain data. Let us denote as the *right and left data* the following sets (where $j = 1, \ldots, k$ and $i = 1, \ldots, q$):

$$\{\lambda_j, \mathbf{r}_j, \mathbf{w}_j\}, \quad \text{and} \quad \{\mu_i, \mathbf{l}_i^\top, \mathbf{v}_i^\top\}, \tag{15}$$

where $\lambda_j \in \mathbb{C}$ and $\mu_i \in \mathbb{C}$ are the right and left interpolation points. Then, $\mathbf{r}_j \in \mathbb{C}^{m\times 1}$ and $\mathbf{l}_i^\top \in \mathbb{C}^{1\times m}$ are the right and left tangential directions. Both points and directions lead to the right $\mathbf{H}(\lambda_j)\mathbf{r}_j = \mathbf{w}_j \in \mathbb{C}^{m\times 1}$ and left $\mathbf{l}_i^\top \mathbf{H}(\mu_i) = \mathbf{v}_i^\top \in \mathbb{C}^{1\times m}$ tangential responses. Let $\mathbf{H}(s_k)$ denote the evaluation of the high dimensional pH-FOM at point $s_k \in \mathbb{C}$. Based on the data sets (15), the LF seeks for a realization $\boldsymbol{\Sigma} : \left(\widehat{E}, \widehat{A}, \widehat{B}, \widehat{C}, 0_m\right)$, whose transfer function $\widehat{\mathbf{H}}(s)$ satisfies tangential interpolatory conditions $\widehat{\mathbf{H}}(\lambda_j)\mathbf{r}_j = \mathbf{w}_j$ and $\mathbf{l}_i^\top \widehat{\mathbf{H}}(\mu_i) = \mathbf{v}_i^\top$. By using the matrix formulation, the right data read:

$$\begin{cases} \Lambda &= \mathbf{diag}\left[\lambda_1, \ldots, \lambda_k\right] \in \mathbb{C}^{k\times k}, \\ R &= \begin{bmatrix} \mathbf{r}_1 & \mathbf{r}_2 & \ldots & \mathbf{r}_k \end{bmatrix} \in \mathbb{C}^{m\times k}, \\ W &= \begin{bmatrix} \mathbf{w}_1 & \mathbf{w}_2 & \ldots & \mathbf{w}_k \end{bmatrix} \in \mathbb{C}^{m\times k}, \end{cases} \tag{16}$$

and the left data read:

$$\begin{cases} M = \mathbf{diag}\,[\mu_1, \ldots, \mu_q] \in \mathbb{C}^{q\times q}, \\ L^\top = \begin{bmatrix} \mathbf{l}_1 & \mathbf{l}_2 & \ldots & \mathbf{l}_q \end{bmatrix} \in \mathbb{C}^{m\times q}, \\ V^\top = \begin{bmatrix} \mathbf{v}_1 & \mathbf{v}_2 & \ldots & \mathbf{v}_q \end{bmatrix} \in \mathbb{C}^{m\times q}. \end{cases} \tag{17}$$

Defining the (i, j) -th entry of the Loewner and shifted Loewner matrices with dimension $q \times k$, as:

$$(\mathbb{L})_{ij} = \frac{\mathbf{v}_i^\top \mathbf{r}_j - \mathbf{l}_i^\top \mathbf{w}_j}{\mu_i - \lambda_j}, \quad \text{and} \quad (\mathbb{M})_{ij} = \frac{\mu_i \mathbf{v}_i^\top \mathbf{r}_j - \mathbf{l}_i^\top \mathbf{w}_j \lambda_j}{\mu_i - \lambda_j}, \tag{18}$$

the resulting system realization $\widehat{\mathbf{\Sigma}} : \left(\widehat{E}, \widehat{A}, \widehat{B}, \widehat{C}, 0_m\right) = (-\mathbb{L}, -\mathbb{M}, V, W, 0_m)$ which transfer function $\widehat{\mathbf{H}}(s) = W(\mathbb{M} - s\mathbb{L})^{-1}V$ (tangentially) interpolates the *data*. Importantly, if the data have been generated by a linear rational model and in the case where too many data are available, both the minimal realization order r and McMillan degree v of the generating system can be obtained. More specifically, $\forall \xi \in \mathbb{C}_\Lambda$, $r = \mathbf{rank}(\xi\mathbb{L} - \mathbb{M}) = \mathbf{rank}([\mathbb{L}, \mathbb{M}]) = \mathbf{rank}([\mathbb{L}^H, \mathbb{M}^H]^H)$, and $v = \mathbf{rank}(\mathbb{L})$. Let $Y \in \mathbb{C}^{q\times r}$ (resp. $X \in \mathbb{C}^{k\times r}$) be the matrix containing the first r left (resp. right) singular vectors of $[\mathbb{L}, \mathbb{M}]$ (resp. $[\mathbb{L}^H, \mathbb{M}^H]^H$). Then, $\widehat{\mathbf{\Sigma}}_r : \left(\widehat{E}_r, \widehat{A}_r, \widehat{B}_r, \widehat{C}_r, 0_m\right)$ where:

$$\widehat{E}_r = Y^H \widehat{E} X, \ \widehat{A}_r = Y^H \widehat{A} X, \ \widehat{B}_r = Y^H \widehat{B} \ \text{ and } \ \widehat{C}_r = CX, \tag{19}$$

is a *minimal realization* that interpolates the data (15). Note that r may be automatically selected by the rank revealing factorization of the LF or be chosen smaller to obtain a simpler function, at the price of a loss of accuracy.

Remark 2. (About the interpolation points and tangential directions). It may be helpful to point out some practical consideration and specificity of the LF:

- The right data λ_j add columns while the left μ_i add rows in the $\mathbb{L}$ and $\mathbb{M}$ matrices (18). It is generally preferred to have a similar number of rows and columns (i.e. k = q = N). If not equal, rectangular matrices may be constructed. After the SVD and projection, square matrices of dimension r are obtained, where r is the rank of the Loewner pencil.
- The left and right points distribution have no impact on the obtained model. For numerical reasons, it is commonly admitted to alternate them. More specifically, assuming k = q = N, if the data of the original model are evaluated at $\{s_1, s_2, \ldots, s_{2N}\} \in \mathbb{C}$, a typical choice for left and right interpolation points is the following (interlacing): $\lambda_{1,2,\ldots,k} = \{s_1, s_3, s_5, \ldots, s_{2N-1}\}$ and $\mu_{1,2,\ldots,q} = \{s_2, s_4, s_6, \ldots, s_{2N}\}$.
- The interpolation points $\{s_1, s_2, \ldots, s_{2N}\}$ may be any point in the complex domain. In practical applications, they are usually collected from frequency response evaluation resulting in interpolation points along the imaginary axis. Therefore, we usually deal with a complex set $\{s_1, s_2, \ldots, s_{2N}\}$ with pure imaginary values only. Then, complex conjugation permit (i) to double the information and (ii) to reconstruct real-valued matrices [see later (29) and (30)].
- The tangential directions $\mathbf{r}_j^\top$ (resp. $\mathbf{l}_i$) may be any complex vectors. Here we suggest to take the right (resp. left) largest singular vector associated the evaluation of the m × m model at λ_j (resp. μ_i). As the interpolation points, they are closed by conjugation.

Remark 3. (Number of interpolation points). Note that the number of ports dictates the number m × m of inputs / outputs for the considered dynamical system. It is generally admitted that the number r of internal variables (or states) needed to catch the dynamics is $r \geq m^2$. This indicates that at least each transfer has its own dynamics. However, this is not always the case and it depends on the involved physics. The strength of the LF used in this work relies on the minimal realization result [see Antoulas et al. (2016) for details, and §5].

4.1.2 Enforcing passivity in the interpolation. In the above presented LF, interpolation is guaranteed while the passivity property may not (indeed, when compression is applied during the SVD step, it is likely to be lost). Authors in Benner *et al.* (2020) provide a solution to this limitation by first using the ROM $\widehat{\mathbf{\Sigma}}_r$ to estimate the associated *spectral zeros and directions pairs*, denoted $(\xi_j, \mathbf{x}_j)$ such that $\mathbf{\Phi}_{\mathbf{H}_r}(\xi_j)\mathbf{x}_j = 0$. This pair is computed by solving the following low order generalized eigenvalue problem:

$$\begin{bmatrix} 0 & \widehat{A}_r & \widehat{B}_r \\ \widehat{A}_r^\top & 0 & \widehat{C}_r^\top \\ \widehat{B}_r^\top & \widehat{C}_r & D + D^\top \end{bmatrix} \begin{pmatrix} p_j \\ q_j \\ \mathbf{x}_j \end{pmatrix} = \xi_j \begin{bmatrix} 0 & \widehat{E}_r & 0 \\ -\widehat{E}_r^\top & 0 & 0 \\ 0 & 0 & 0 \end{bmatrix} \begin{pmatrix} p_j \\ q_j \\ \mathbf{x}_j \end{pmatrix}, \tag{20}$$

which has *r* zeros in the open right half-plane, *r* zeros in the open left half-plane and has no zeros on the imaginary axis. Now by selecting the *right and left strictly passive data* data as ($i, j = 1, \ldots, r = k = q, \lambda_j \leftarrow \xi_j$ and $\mathbf{r}_j \leftarrow \mathbf{x}_i$):

$$\{\lambda_j, \mathbf{r}_j, \mathbf{w}_j\} \text{ and } \{-\overline{\lambda}_i, \mathbf{r}_i^H, -\mathbf{w}_i^H\}, \tag{21}$$

one gets, $M = -\Lambda^H$, $L = R$ and $V = -W^H$. By construction, one obtains Hermitian $\mathbb{L} \in \mathbb{C}^{r\times r}$ and a skew symmetric $\mathbb{M} \in \mathbb{C}^{r\times r}$ matrices (18). By setting, $\mathbf{H}(\infty) = D$ (which may be estimated by measuring in very high frequency if not accessible), one recovers a $m \times m$ passive realization $\widehat{\mathbf{\Sigma}}_p = (-\mathbb{L}, -\mathbb{M}, -W^H, W, 0_m) := \left(\widehat{E}_p, \widehat{A}_p, \widehat{B}_p, \widehat{C}_p, 0_m\right)$. As $\mathbb{L} \succ 0$, one may apply the Cholesky decomposition $\mathbb{L} = T^\top T$ (and the Loewner matrix can easily be inverted). Then the *normalized pH-ROM* is obtained as $\widehat{\mathbf{\Sigma}}_{\mathrm{n-pH}} := \left(I_r, T\widehat{A}_p T^{-1}, T\widehat{B}_p, \widehat{C}_p T^{-1}, D\right)$ (Mehrmann and Van Dooren, 2020; Benner *et al.*, 2020), with form (1b). Defining:

$$S := \begin{bmatrix} -T\widehat{A}_p T^{-1} & -T\widehat{B}_p \\ \widehat{C}_p T^{-1} & D \end{bmatrix}, \tag{22}$$

one obtains the equivalent pH-ROM of the form (1c) by identifying:

$$\begin{bmatrix} -J & -G \\ G^\top & N \end{bmatrix} := \frac{S - S^\top}{2}, \text{ and } \begin{bmatrix} R & P \\ P^\top & S \end{bmatrix} := \frac{S + S^\top}{2}, \tag{23}$$

which now leads to the *r*-th order normalized pH-ROM shortly denoted $\widehat{\mathbf{\Sigma}}_{\mathrm{pH}}$ in the form (1c).

Remark 4. (About spectral zeros interpolation). Notice that the spectral zeros embed the passivity property. One manner to preserve passivity is then by interpolation along spectral

zeros and directions. In Poussot-Vassal et al. (2023), a procedure ensuring stability and avoiding numerical issues is detailed.

4.2 The interest in having a port-Hamiltonian reduced-order model

The r-th order pH-ROM $\widehat{\mathbf{\Sigma}}_{\text{pH}}$ in the form (1c), is a $m \times m$ MIMO model that captures well the behaviors of the pH-FOM (in a non-intrusive manner). Moreover, as $\widehat{\mathbf{\Sigma}}_{\text{pH}}$ is *normalized*, the r internal variables allow for the reconstruction of energy and power terms of the ROM, mirroring those of the original full-order model. These terms are computed as follows:

$$\begin{aligned}
&\text{Hamiltonian or internal energy} : \mathcal{E}^r(t) = \widehat{\mathbf{x}}_r(t)^\top \widehat{\mathbf{x}}_r(t),\\
&\text{Internal dissipated power} : \widehat{\mathbf{x}}_r(t)^\top (J-R)\widehat{\mathbf{x}}_r(t) = -\widehat{\mathbf{x}}_r(t)^\top R \widehat{\mathbf{x}}_r(t),\\
&\text{Exchange power} : u(t)^\top \widehat{y}(t).
\end{aligned} \tag{24}$$

These considerations will be explored in §5, and illustrated on Figure 6.

4.3 Associated projectors

In addition, an interesting property rarely exploited in model reduction works, concerns the Loewner projectors, constructed with the FOM knowledge, and the considered interpolations points (λ_j, μ_i) and directions ($\mathbf{r}_j$, $\mathbf{l}_j$). Thanks to these quantities, it is possible to reconstruct (approximate) the pH-FOM internal variables on the basis of the pH-ROM ones thanks to the *lifting* operator:

$$\mathbf{x}(t) = V\widehat{\mathbf{x}}_r(t), \tag{25}$$

where $\widehat{\mathbf{x}}_r(t)$ and $\mathbf{x}(t)$ are the internal state variables of the pH-ROM and pH-FOM, respectively. Then, the $V \in \mathbb{R}n^{\times r}$ matrix is the so-called lifting projector, defined in what follows. From the Loewner theory, see Antoulas *et al.* (2016), the Loewner and shifted Loewner matrices satisfy:

$$\mathcal{O}E\mathcal{R} = \mathbb{L} \quad \text{and} \quad \mathcal{O}A\mathcal{R} = \mathbb{M}, \tag{26}$$

where the generalized observably and reachability matrices read (by considering that the interpolation points and directions are closed by conjugation):

$$\mathcal{R} = \begin{bmatrix} \mathbf{r}_1^\top B^\top (\lambda_1 E - A)^{-\top} \\ \overline{\mathbf{r}}_1^T B^\top \left(\overline{\lambda}_1 E - A\right)^{-\top} \\ \vdots \\ \mathbf{r}_{k/2}^\top B^\top \left(\lambda_{k/2} E - A\right)^{-\top} \\ \overline{\mathbf{r}}_{k/2} B^\top \left(\overline{\lambda}_{k/2} E - A\right)^{-\top} \end{bmatrix} \quad \text{and} \quad \mathcal{O} = \begin{bmatrix} \mathbf{l}_1 C(\mu_1 E - A)^{-1} \\ \overline{\mathbf{l}}_1 C(\overline{\mu}_1 E - A)^{-1} \\ \vdots \\ \mathbf{l}_{q/2} C\left(\mu_{q/2} E - A\right)^{-1} \\ \overline{\mathbf{l}}_{q/2} C\left(\overline{\mu}_{q/2} E - A\right)^{-1} \end{bmatrix}. \tag{27}$$

The above relation means that the shifted Loewner and Loewner matrices are projection of the A and E matrices onto the generalized observability and reachability spaces. Then, as $\mathcal{R}$ and $\mathcal{O}$ are complex but closed by conjugation, the following equality holds true (for $q = k = r$):

$$\begin{aligned}(Y^\top J^H \mathcal{O})^\top E(\mathcal{R}JX) &= \mathbb{L},\\ (Y^\top J^H \mathcal{O})^\top A(\mathcal{R}JX) &= \mathbb{M},\end{aligned} \tag{28}$$

where:

$$J_0 = \frac{1}{\sqrt{2}}\begin{bmatrix}1 & \imath\\ 1 & -\imath\end{bmatrix} \text{ and } J = I_{k/2} \otimes (J_0 \otimes I_m), \tag{29}$$

and where:

$$\widetilde{Y}\Sigma X = \mathbf{SVD}\begin{bmatrix}\mathbb{M}\\ \mathbb{L}\end{bmatrix} \text{ and } Y\Sigma\widetilde{X} = \mathbf{SVD}\begin{bmatrix}\mathbb{M} & \mathbb{L}\end{bmatrix}. \tag{30}$$

Then, we define the projectors as:

$$W = Y^\top J^H \mathcal{O} \text{ and } V = \mathcal{R}JX. \tag{31}$$

The $V \in \mathbb{R}n^{\times r}$ will serve in (25) to lift the pH-ROM states up to the pH-FOM (refer to §5 for illustrations).

Remark 5. (About numerical improvements). Once the equivalent projecting matrices (31) have been obtained, it may also be interesting to improve the numerical conditioning. This is possible e.g. by applying the balanced transformation on the normalized pH model. Then, the projectors read [where $T_R \in \mathbb{R}^{r\times r}$ *and* $T_L \in \mathbb{R}^{r\times r}$ denote the right and left projectors of the balancing, see Antoulas *et al.* (2016)]:

$$W = T_R Y^\top J^H \mathcal{O}, \quad \text{and} \quad V = \mathcal{R}JXT_L, \tag{32}$$

and ensure $W^\top EV = \mathbb{L}$ *and* $W^\top AV = \mathbb{M}$.

5. Test case: a waveguide

This section aims to demonstrate the effectiveness of the above method in handling complex material properties. Therefore, in Figure 2, we consider a waveguide composed of three regions structured as follows: the first region is empty space with $\epsilon_1 = 1$, $\mu_1 = 1$ and $\sigma_1 = 0$, the second region contains a material with conductivity, i.e. $\epsilon_2 = 5$, $\mu_2 = 1$ and $\sigma_2 = 5$, and the third region is again the same empty space. Note that these parameters are not physically speaking since the system has been a-dimensioned. The complexity of the waveguide arises from the discontinuous

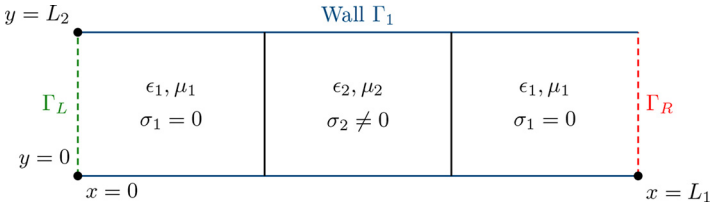

Figure 2. Geometry of the waveguide under consideration
Source: Authors' own work

physical properties at the interfaces between the regions. These discontinuities lead to abrupt changes in the electromagnetic field behavior, making the analysis and simulation of the waveguide more challenging. For simplicity sake, in the study the empty space electromagnetic properties are normalized to one. This consideration results in analyzing model responses on a normalized frequency axis.

For this test case, we have chosen a simulation domain with reasonable dimensions $\Omega = [0, 1] \times [0, 0.1]$. As will be seen later, this choice of domain already results in a full-order model with significant dimensions. On the top and bottom boundaries (Γ_1), a zero electric field is imposed as boundary condition. The left and right boundaries ($\Gamma_2 = \Gamma_L \cup \Gamma_R$) will be the collocated inputs and outputs. Here, the control is chosen to be the tangent component of the electric field to the boundary Γ_2. Thus, the collocated observation is necessarily $-H_z$ on Γ_2, in accordance with the port-Hamiltonian formalism presented § 2. Equations (33) display the final formulation:

$$\begin{cases} \dfrac{\partial}{\partial t}\begin{pmatrix} \epsilon \mathbf{E} \\ \\ \mu H_z \end{pmatrix} = (J-R)\begin{pmatrix} \mathbf{E} \\ \\ H_z \end{pmatrix}, & \text{on } \Omega, \\ \mathbf{E}\cdot\mathbf{t} = 0, & \text{on } \Gamma_1, \\ \mathbf{E}\cdot\mathbf{t} = u_\partial, & \text{on } \Gamma_2 = \Gamma_L \cup \Gamma_R, \\ y_\partial = -H_z, & \text{on } \Gamma_2 = \Gamma_L \cup \Gamma_R. \end{cases} \tag{33}$$

The finite element implementation and the time simulation of the FOM were conducted using the SCRIMP (Simulation and Control of Interactions in Multi-Physics) library, see Ferraro *et al.* (2024), which is specifically designed for port-Hamiltonian systems. Numerous examples are available on the SCRIMP web page https://g-haine.github.io/scrimp/. One of the main advantages of this library is its ability to track the Hamiltonian terms over time. The finite element families used for the FOM are as follows:

- vectorial Discontinuous Galerkin of order 1 for $\boldsymbol{E}$;
- scalar Continuous Galerkin of order 2 for H_z; and
- scalar Discontinuous Galerkin of order 1 for both u_∂ and y_∂ at the boundary.

These choices have been made in accordance with the matrices of (11). Indeed, only the D and T matrices involve operators that need φ to belong at least to $H^1(\Omega)$, respectively $\mathbf{grad}^\perp$ and γ. Furthermore, it is well-known that the gradient of Continuous Galerkin elements of order k is mapped to vectorial Discontinuous Galerkin elements of order $k-1$, which ensures an optimal compatibility, see Haine *et al.* (2023) for details.

Figure 3 presents the results obtained with a Gaussian pulse wave injected at the left boundary of the domain. As power is introduced into the system (pink curve), the electromagnetic energy increases in the domain (dark green curve). When the injected wave reaches the second material, fluctuations appear on the electric and magnetic terms. Additionally, the total electromagnetic energy gradually decreases due to the Joule effect caused by the non-zero conductivity of second material. This phenomenon is also modeled by the plot of the damping term $\int_0^T -\underline{E}(t)^\top R_\sigma \underline{E}(t) dt$ (light grey curve). Finally, the power-balance equation remains at zero throughout the simulation, thereby validating equation (14) (light green curve).

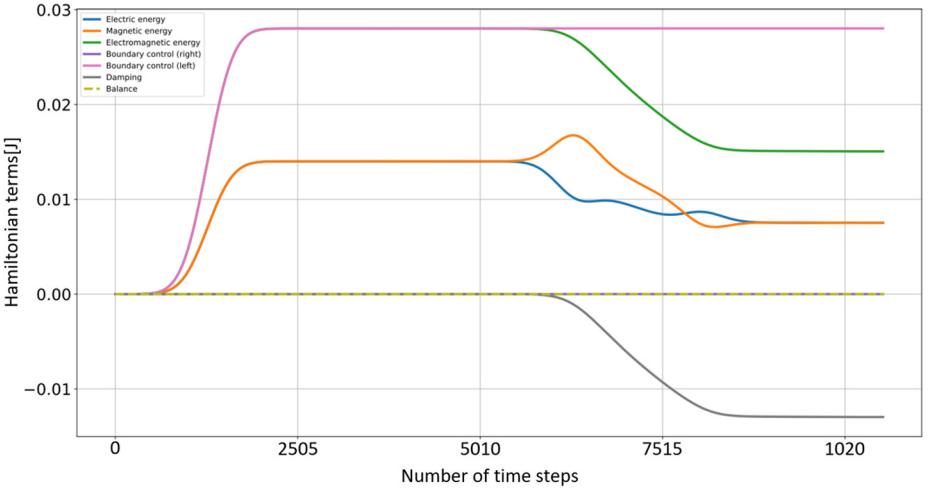

Figure 3. Evolution of the terms of the Hamiltonian in plain lines [electric energy (blue), magnetic energy (orange), electromagnetic energy (green), right boundary control (purple), left boundary control (pink), damping (gray) and power balance in dashed line (yellow)]
Source: Authors' own work

5.1 Computation of the reduced-order models

As presented in § 4, obtaining reduced-order models is of great value. However, we aim to preserve the port-Hamiltonian formalism throughout the process. The finite element model obtained above stands for FOM. As Loewner framework is based on frequency interpolation, we need to compute frequency response of the FOM. To do this, the transfer function of the FOM is constructed by performing a Laplace transformation of (12)–(13):

$$\mathbf{H}(s) = G^{\top}(sM - (J - R))^{-1}G.$$

The state and ports dimension of the FOM is $n = 733$ $m = 8$ for a large mesh size. Then, 500 evaluation of the FOM are computed, as follows:

$$\{\omega_1, \omega_2, \ldots, \omega_{500}\} = \texttt{logscale}\left[10^{-3}, 10^{1}\right]$$

$$\{\lambda_1, \overline{\lambda_1}, \lambda_2, \overline{\lambda_2}, \ldots, \lambda_{250}, \overline{\lambda_{250}}\} = \imath\{\omega_1, \overline{\omega_1}, \omega_3, \overline{\omega_3}, \ldots, \omega_{499}, \overline{\omega_{499}}\}$$

$$\{\mu_1, \overline{\mu_1}, \mu_2, \overline{\mu_2}, \ldots, \mu_{250}, \overline{\mu_{250}}\} = \imath\{\omega_2, \overline{\omega_2}, \omega_4, \overline{\omega_4}, \ldots, \omega_{500}, \overline{\omega_{500}}\},$$

leading to a tangential Loewner interpolant of size $r = 21$ after reduction. However, this ROM is not passive, thus preventing its transformation in the pH structure. Passivity of the interpolant can be enforced, following Benner *et al.* (2020) procedure recalled in § 4. The main idea of the method is to use spectral zeros as interpolating points. Nevertheless, this algorithm works only for strictly passive systems that allow an easy selection of positive spectral zeros.

In our case, due to the complexity and significant size of finite models, some numerical issues prevent us from directly using this method. Indeed, the computation of spectral zeros is challenging for large systems. Moreover, our systems are non-strictly passive due to weak

damping, thus spectral zeros can be found close to the imaginary axis. To solve these numerical problems, the algorithm in Poussot-Vassal *et al.* (2023) suggests shifting the measured data using the D matrix of the state-space formulation (interested reader is invited to refer to §II.C of this article). In SISO, the effect of this operation is easy to observe. It consists of translating the Nyquist plot to the right part of the domain to enforce strict passivity. Once a passive ROM is identified that fits the shifted data, we just need to shift it back to make it fit the initial model.

In practice, a sensitivity analysis has been conducted on the D term, since this parameter influences the number of numerically computed spectral zeros. If any are missed during computation, critical information can be lost and the final solution will not accurately reflect the behavior of the full-order model (FOM). For this particular case, the optimal D term value is around 10^{-2}.

We end up with two reduced order models: $\widehat{\boldsymbol{\Sigma}}$ and $\widehat{\boldsymbol{\Sigma}}_{\text{pH}}$ of size $r = 21$, because $\widehat{\boldsymbol{\Sigma}}_{\text{pH}}$ is computed from positive spectral zeros of $\widehat{\boldsymbol{\Sigma}}$, which are exactly $r = 21$ thanks to the shift action. The resulting ROMs are therefore almost 35 times smaller than the FOM. Figure 4 shows the frequency responses of the two computed ROMs. Due to space limitation, we only show the magnitude of two transfer functions relating the mean left and right outputs (Y_L and Y_R) to the mean right and left inputs (U_L and U_R). As expected, the two ROM responses are close to the one of full order model near the frequencies selected from the interpolated data and spectral zeros.

The fact that our ROMs do not match the high-frequency FOM response is not necessarily a problem. It is important to think about the measurement frequency range we use for the interpolation. Indeed, our finite element model will not be able to capture very high frequency behavior. This limitation is due to the inherent limitations of the finite element method and the discretization used in our model. High frequency signals have shorter wavelengths that require finer meshes to accurately capture their behavior. In the next part, the effect of this partial matching on the frequency responses is shown on a time-domain simulation.

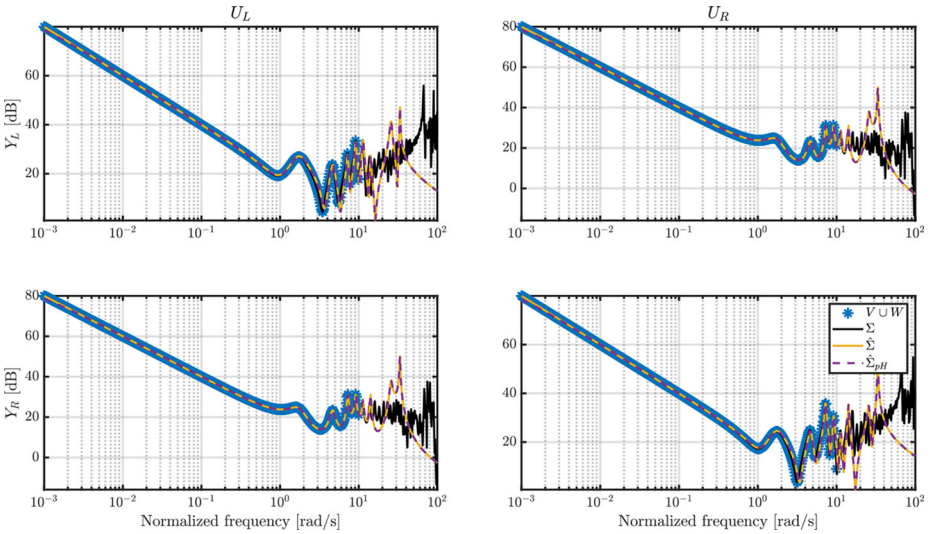

Figure 4. Magnitude Bode diagram of the FOM $\sum$, Loewner ROM $\widehat{\boldsymbol{\Sigma}}$ and pH-ROM $\widehat{\boldsymbol{\Sigma}}_{\text{pH}}$ with selected interpolated data $V \bigcup W$

Source: Authors' own work

5.2 Simulation results in the time domain

Figure 5 shows the evolution of the outputs of three models in response to a sinusoidal wave injected at the left boundary of the domain. The time required to compute the solution using the FOM is 59.57 s, whereas the ROMs calculate the solution in just 0.67 s. This results in a significant speedup, with the ROMs being approximately 89 times faster than the FOM. This substantial reduction in computation time highlights the efficiency of the ROMs, making them highly advantageous for scenarios where rapid simulations are essential without sacrificing too much accuracy.

The evolution of the output Y_L on the left boundary Γ_L is accurately captured by both ROMs, as it corresponds to the collocated output of U_L, which is less complex to model. For the output Y_R measured on the right boundary Γ_R, the FOM accurately reflects the delay caused by wave propagation along the waveguide. However, this delay is not well captured by the ROMs due to the truncation of high-frequency components during the reduction process. However, increasing the ROM order may improve this, at the price of a more complex model.

The mean normalized error for $\widehat{\mathbf{\Sigma}}$ is 0.0857, while for $\widehat{\mathbf{\Sigma}}_{\text{pH}}$ it is 0.0905 (the error has been normalized to the maximum output value). These errors remain low, which validates the time-domain behavior of both ROMs. It is important to note that the characteristics of the injected signal significantly influences the output shapes. Inputs with sharp transitions or high-frequency components can introduce considerable numerical noise, potentially affecting the accuracy of the model predictions. Therefore, while the ROMs perform well under the current conditions, care must be taken when applying these models to more complex input signals, as they may lead to less accurate results due to the presence of unresolved high-frequency behavior. This is to be studied in future works.

One of the main advantages of the port-Hamiltonian formalism is its ability to track the evolution of the Hamiltonian, which, in this context, represents the internal electromagnetic

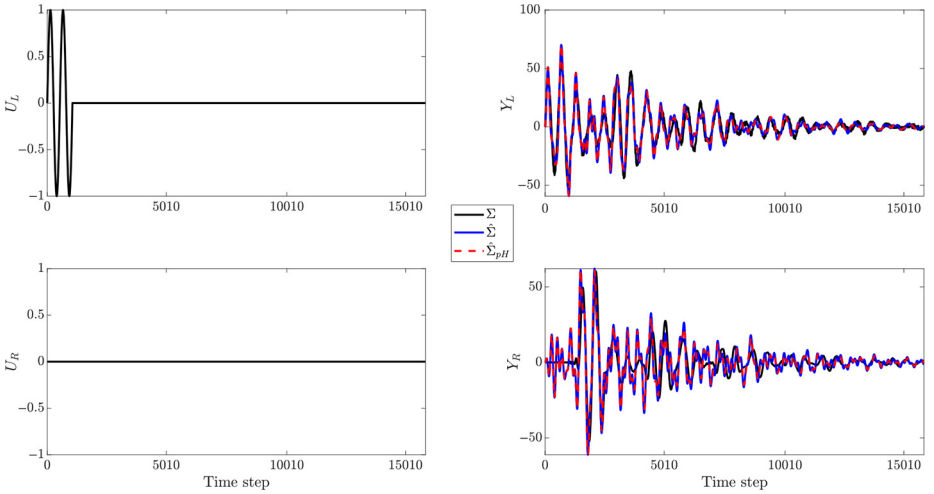

Figure 5. Time-domain responses for sinusoidal input at left boundary of the domain. On the bottom right frame, the delay is not well captured by the rational form, but may be improved by increasing the order r

Source: Authors' own work

energy. Additionally, it allows for the straightforward plotting of exchange power, internal damping, and power balance check equations. Equation (9) shows the method for calculating these terms for the FOM. For $\widehat{\mathbf{\Sigma}}_{\text{pH}}$, since it is represented as a normalized port-Hamiltonian system, these terms can be easily calculated as described at the beginning of §4.3. Figure 6 displays these curves for both the FOM and the port-Hamiltonian pH-ROM ($\widehat{\mathbf{\Sigma}}_{\text{pH}}$). The power balance equation is satisfied for both models, with the exchange power terms showing good agreement. However, there are differences in the damping terms which affect the rate of decrease of the electromagnetic energy. In particular, the pH-ROM appears to be less dissipative than the FOM. This is a direction to be investigated as it might be induced by the time integration scheme.

Remark 6. (Time-domain). All variables used in the simulation are a-dimensioned. Therefore in all above simulations, neither the rad/s nor time duration have a specific meaning.

5.3 Projection of the reduced state on the mesh

Following §4.3, projectors can be computed to project the solutions of the ROM states onto the original mesh. This powerful approach provides a more detailed understanding of the internal behavior of the ROMs, allowing for a closer examination of how well they capture the dynamics of the full-order model. Figure 7 shows the internal state evolution of the FOM and the reconstructed state of the pH-ROM. The propagation behavior is well reconstructed by the pH-ROM even after many time steps, as can be seen on Figure 7c. Indeed, pH-ROM effectively captures both reflection and transmission phenomena at interfaces.

Once again, we choose to normalize the error at time t by the highest value of the magnetic field at the same time, because H converges to zero. In the center of the waveguide, the error remains small, but reconstruction at the left and right boundaries is more problematic, with significant differences appearing. Nevertheless, we saw in Figure 5 that the opposite of the magnetic field as output of the system is well fitted by $\widehat{\mathbf{\Sigma}}_{\text{pH}}$. It is therefore possible to replace the magnetic field value reconstructed with projectors by the one calculated by $\widehat{\mathbf{\Sigma}}_{\text{pH}}$, allowing better reconstruction of the field.

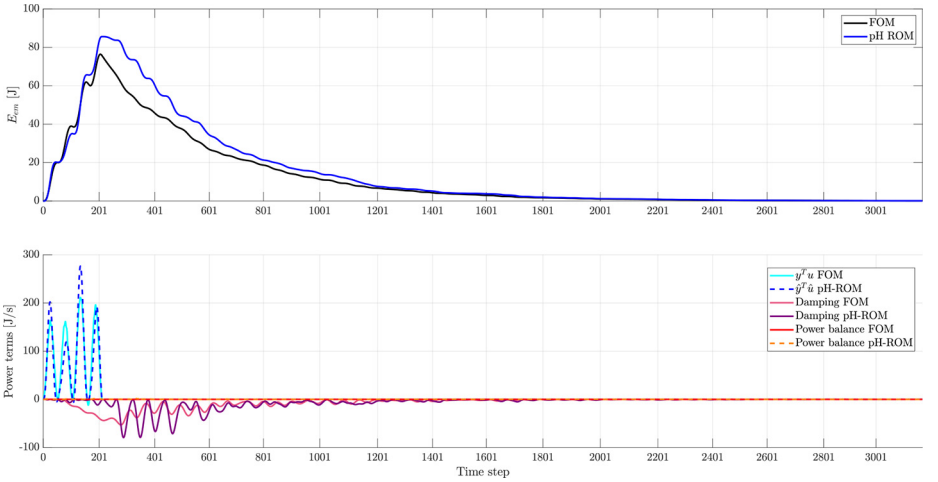

Figure 6. Hamiltonian, energy terms and power balance of the FOM and pH-ROM ($\widehat{\mathbf{\Sigma}}_{\text{pH}}$)
Source: Authors' own work

In this section, we have chosen the smallest possible model to demonstrate the power of model reduction. This choice is associated with limited accuracy because, as mentioned above, the high frequency behavior has been truncated. Better accuracy can be achieved with a larger model. For example, Figure 1 displays the reconstructed magnetic and electric fields obtained with a ROM twice as large, of dimension $r = 55$.

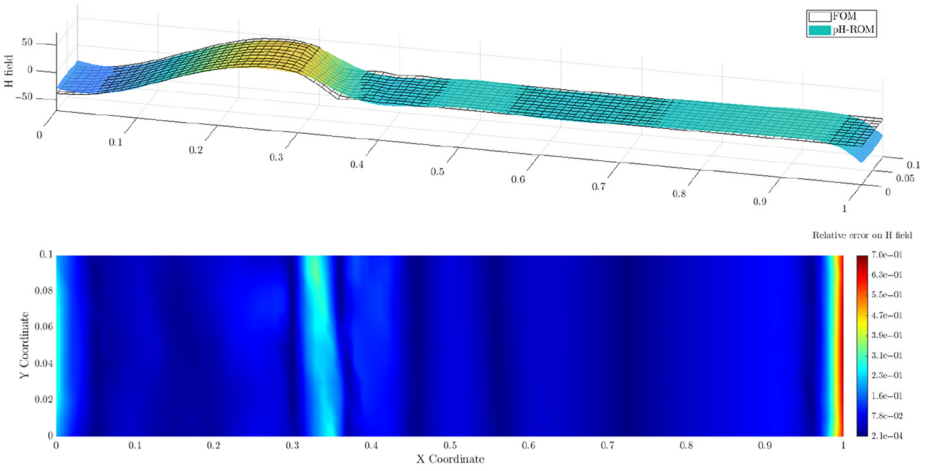

(a) At time step 401.

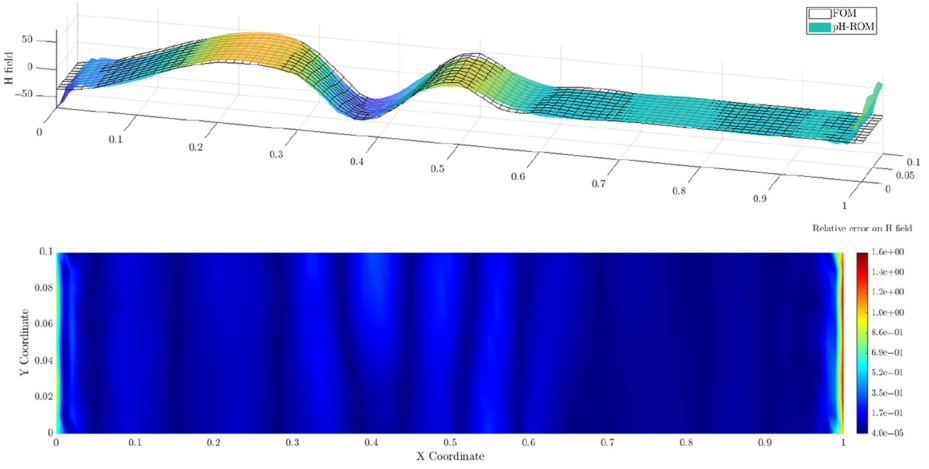

(b) At time step 900.

Figure 7. Results of the reconstruction of the reduced state on the initial mesh, comparison with time response of the FOM. At each time step, the top subplot represents the H_z field in black for the FOM and in colors for the pH-ROM ($r = 21$), and the bottom subplot is the relative error on the H_z field
Note(s): (a) At time step 401; (b) at time step 900; (c) at time step 1350
Source: Authors' own work

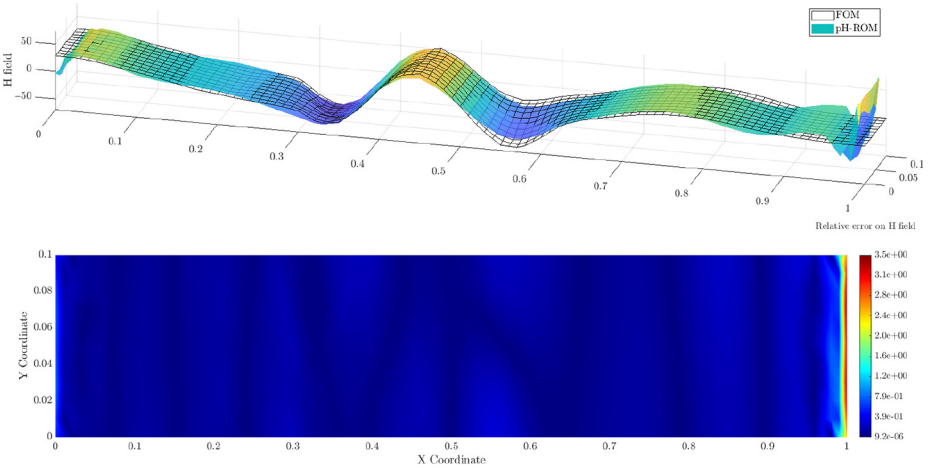

(c) At time step 1350.

Figure 7. Continued

6. Conclusion and outlook

This work presented a systematic approach to the modeling and order reduction of the 2D Maxwell equations within a port-Hamiltonian framework. We demonstrated that the Loewner method effectively reduces simulation complexity, while preserving the intrinsic structure of port-Hamiltonian systems. The simulation results showed that the obtained reduced-order models faithfully reproduce the input-output system; furthermore the dynamic behavior of the full-order model is recovered thanks to a specific lifting operator, resulting in a significant reduction in computational time.

The importance of preserving the port-Hamiltonian structure throughout the three steps of modeling, discretization, and reduction has been demonstrated, as this structure allows the easy computation of essential power terms, providing a great understanding of the computed models from an energy perspective. Moreover, the passivity property that naturally comes with the structure is of major interest, as it enables the implementation of passivity-based controllers (not treated here), robust to high uncertainties and perturbations. In addition, natural Lyapunov functions proving the exponential stability of a port-Hamiltonian system can be simply derived from its state and its Hamiltonian. Consequently, the port-Hamiltonian theory provides a perfect framework for the control of continuous domain and complex phenoma.

To summarize, along with a method to compute a pH-ROM from PDEs, essential tools have been proposed in this work to take full advantage of a pH-reduced order model, offering a deep understanding of the initial full order model, such as frequency response, time response, energy and power term computation, and reconstruction of the response on the initial mesh.

Future perspectives include applying this methodology to more complex electromagnetic system configurations, which would be an interesting step forward to validate and extend this approach in practical applications such as those coming from multiport array antennas. Addressing the parametrized 3D case represents an important challenge for real-life applications; to fully address this case, numerical issues would need to be treated, including

the evaluation of the frequency-domain response evaluation, the data storage and the potential high number of ports. A thorough exploration of dedicated techniques to enhance the passivity and transport delay accuracy of ROMs also in the high-frequency band would also be beneficial, following e.g. Toledo-Zucco *et al.* (2024a).

COMPEL - The international journal for computation and mathematics in electrical and electronic engineering

Notes

1. This work has been supported by the AID (Agence de l'Innovation de Défense) from the French Ministry of the Armed Forces (Ministère des Armées).

2. see https://g-haine.github.io/scrimp/.

3. Here Λ denotes the singularities being the eigenvalues of (A, E) pencil in (1a), of A in (1b) and of $((J - R)Q, M)$ in (1c).

4. Note that both these adjoint operators do also naturally come into play in the case of the 2D incompressible Navier-Stokes equations written as a pHs with vorticity as energy variable, see Haine and Matignon (2021) and Cardoso-Ribeiro *et al.* (2024).

References

Antoulas, A.C., Beattie, C.A. and Gugercin, S. (2020), "Interpolatory methods for model reduction", *Computational Science and Engineering*, SIAM, PA.

Antoulas, A.C., Lefteriu, S. and Ionita, A.C. (2016), "Chapter a tutorial introduction to the Loewner framework for model reduction", in Benner, P., Cohen, A., Ohlberger, M. and Willcox, K. (Eds), *Model Reduction and Approximation Theory and Algorithms*, SIAM, PA.

Assous, F., Ciarlet, P. and Labrunie, S. (2018), *Mathematical Foundations of Computational Electromagnetism*, Springer, Cham.

Bartel, A. and Günther, M. (2018), "PDAEs in refined electrical network modeling", *SIAM Review*, Vol. 60 No. 1, pp. 56-91.

Bartel, A., Clemens, M., Günther, M., Jacob, B. and Reis, T. (2024), "Port-Hamiltonian systems' modelling in electrical engineering", in van Beurden, M., Budko, N.V., Ciuprina, G., Schilders, W., Bansal, H. and Barbulescu, R. (Eds), *Scientific Computing in Electrical Engineering*, Springer Nature Switzerland, Cham, pp. 133-143.

Benner, P., Goyal, P. and Van Dooren, P. (2020), "Identification of port-Hamiltonian systems from frequency response data", *Systems and Control Letters*, Vol. 143, p. 104741.

Benner, P., Gugercin, S. and Willcox, K. (2015), "A survey of projection-based model reduction methods for parametric dynamical systems", *SIAM Review*, Vol. 57 No. 4, pp. 483-531.

Bundschuh, J., Ruppert, M. and Späck-Leigsnering, Y. (2023), "Pyrit: a finite element based field simulation software written in Python", *COMPEL - The International Journal for Computation and Mathematics in Electrical and Electronic Engineering*, Vol. 42 No. 5, pp. 1007-1020.

Cardoso-Ribeiro, F., Matignon, D. and Lefèvre, L. (2021), "A partitioned finite-element method for power-preserving discretization of open systems of conservation laws", *IMA Journal of Mathematical Control and Information*, Vol. 38 No. 2, pp. 493-533.

Cardoso-Ribeiro, F.L., Haine, G., Le Gorrec, Y., Matignon, D. and Ramirez, H. (2024), "Port-Hamiltonian formulations for the modeling, simulation and control of fluids", *Computers and Fluids*, Vol. 283, p. 106407.

Cherifi, K. and Brugnoli, A. (2021), "Application of data-driven realizations to port-Hamiltonian flexible structures", *In IFAC-PapersOnLine*, Vol. 54 No. 19, pp. 180-185.

Ciuprina, G., Ioan, D. and Sabariego, R. (2022), "Electric circuit element boundary conditions in the finite element method for full-wave passive electromagnetic devices", *Journal of Mathematics in Industry*, Vol. 12 No. 1.

Clemens, M. and Weiland, T. (2001), "Discrete electromagnetism with the finite integration technique", *Progress in Electromagnetics Research*, Vol. 32, pp. 65-87.

Condon, M. (2024), "Simulation of nonuniform transmission lines", *COMPEL - The International Journal for Computation and Mathematics in Electrical and Electronic Engineering*, Vol. 43 No. 1, pp. 1-13.

Farle, O., Klis, D., Jochum, M., Floch, O. and Dyczij-Edlinger, R. (2013), "A port-Hamiltonian finite-element formulation for the Maxwell equations", *2013 International Conference on Electromagnetics in Advanced Applications (ICEAA)*, pp. 324-327.

Ferraro, G., Fournié, M. and Haine, G. (2024), "Simulation and control of interactions in multi-physics, a python package for port-Hamiltonian systems", *IFAC-PapersOnLine*, Vol. 58 No. 6, pp. 119-124.

Gernandt, H., Haller, F., Reis, T. and van der Schaft, A. (2021), "Port-Hamiltonian formulation of nonlinear electrical circuits", *Journal of Geometry and Physics*, Vol. 159, p. 103959.

Gosea, I.V., Poussot-Vassal, C. and Antoulas, A.C. (2022), "Data-driven modeling and control of large-scale dynamical systems in the Loewner framework", *Handbook of Numerical Analysis*, Vol. 23, pp. 499-530.

Haine, G. and Matignon, D. (2021), "Incompressible Navier-Stokes equation as port-Hamiltonian systems: velocity formulation versus vorticity formulation", *IFAC-PapersOnLine*, Vol. 54 No. 19, pp. 161-616.

Haine, G., Matignon, D. and Monteghetti, F. (2022), "Structure-preserving discretization of Maxwell's equations as a port-Hamiltonian system", *In IFAC-PapersOnLine*, Vol. 55 No. 30, pp. 424-429.

Haine, G., Matignon, D. and Serhani, A. (2023), "Numerical analysis of a structure-preserving space-discretization for an anisotropic and heterogeneous boundary controlled N-dimensional wave equation as a port-Hamiltonian system", *International Journal of Numerical Analysis & Modeling*, Vol. 20 No. 1, pp. 92-133.

Márquez, F.M., Zufiria, P.J. and Yebra, L.J. (2020), "Port-Hamiltonian modeling of multiphysics systems and object-oriented implementation with the modelica language", *IEEE Access*, Vol. 8, pp. 105980-105996.

Mayo, A.J. and Antoulas, A.C. (2007), "A framework for the solution of the generalized realization problem", *Linear Algebra and Its Applications*, Vol. 425 Nos 2/3, pp. 634-662.

Mehrmann, V. and Van Dooren, P. (2020), "Optimal robustness of port-Hamiltonian systems", *SIAM Journal on Matrix Analysis and Applications*, Vol. 41 No. 1, pp. 134-151.

Monk, P. (2003), *Finite Element Methods for Maxwell's Equations*, Oxford University Press, Oxford.

Payen, G., Matignon, D. and Haine, G. (2020), "Modelling and structure-preserving discretization of Maxwell's equations as port-Hamiltonian system", *In IFAC-PapersOnLine*, Vol. 53 No. 2, pp. 7581-7586.

Poussot-Vassal, C., Matignon, D., Haine, G. and Vuillemin, P. (2023), "Data-driven port-Hamiltonian structured identification for non-strictly passive systems", Proc. European Control Conference (ECC), *Bucharest, Romania*, pp. 1785-1790.

Rashad, R., Califano, F., van der Schaft, A. and Stramigioli, S. (2020), "Twenty years of distributed port-Hamiltonian systems: a literature review", *IMA Journal of Mathematical Control and Information*, Vol. 37 No. 4, pp. 1400-1422.

Toledo-Zucco, J.-P., Matignon, D. and Poussot-Vassal, C. (2024a), "Scattering-passive structure-preserving finite element method for the boundary controlled transport equation with a moving mesh", *In IFAC-PapersOnLine*, Vol. 58 No. 6, pp. 292-297.

Toledo-Zucco, J.-P., Matignon, D., Poussot-Vassal, C. and Le Gorrec, Y. (2024b), "Structure-preserving discretization and model order reduction of boundary-controlled 1D port-Hamiltonian systems", *Systems and Control Letters*, Vol. 194, p. 105947.

van der Schaft, A. and Maschke, B. (2002), "Hamiltonian formulation of distributed-parameter systems with boundary energy flow", *Journal of Geometry and Physics*, Vol. 42 Nos 1/2, pp. 166-194.

Weiss, G. and Staffans, O.J. (2013), "Maxwell's equations as a scattering passive linear system", *SIAM Journal on Control and Optimization*, Vol. 51 No. 5, pp. 3722-3756.

Corresponding author
Ghislain Haine can be contacted at: ghislain.haine@isae-supaero.fr

COMPEL - The international journal for computation and mathematics in electrical and electronic engineering